

Journal Pre-proof

The research on CO oxidation over Ce–Mn oxides: The preparation method effects and oxidation mechanism

Zhiping Ye, Yang Liu, Anton Nikiforov, Jiayu Ji, Bo Zhao, Jiade Wang



PII: S0045-6535(23)01397-8

DOI: <https://doi.org/10.1016/j.chemosphere.2023.139130>

Reference: CHEM 139130

To appear in: *ECSN*

Received Date: 7 February 2023

Revised Date: 2 June 2023

Accepted Date: 3 June 2023

Please cite this article as: Ye, Z., Liu, Y., Nikiforov, A., Ji, J., Zhao, B., Wang, J., The research on CO oxidation over Ce–Mn oxides: The preparation method effects and oxidation mechanism, *Chemosphere* (2023), doi: <https://doi.org/10.1016/j.chemosphere.2023.139130>.

This is a PDF file of an article that has undergone enhancements after acceptance, such as the addition of a cover page and metadata, and formatting for readability, but it is not yet the definitive version of record. This version will undergo additional copyediting, typesetting and review before it is published in its final form, but we are providing this version to give early visibility of the article. Please note that, during the production process, errors may be discovered which could affect the content, and all legal disclaimers that apply to the journal pertain.

© 2023 Published by Elsevier Ltd.

Zhiping Ye: Writing - Original Draft, Validation, Formal analysis, Visualization, Methodology

Data curation, Investigation, Conceptualization.

Yang Liu: Writing - Original Draft, Data Curation, Validation, Formal analysis, Visualization,

Investigation.

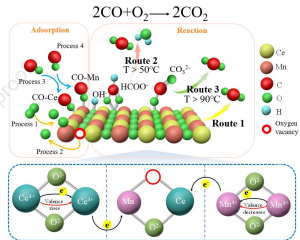
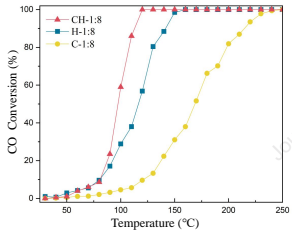
Anton Nikiforov: Writing – review & editing, Validation, Software, Funding acquisition

Jiayu Ji: Resources, Visualization, Investigation, Formal analysis, Validation.

Bo Zhao: Resources, Writing – review & editing, Supervision, Funding acquisition.

Jiade Wang : Methodology, Writing - Review &Editing, Funding acquisition, Resources,

Supervision, Project administration.



1 **The research on CO oxidation over Ce-Mn oxides: the preparation method effects and oxidation**
2 **mechanism**

3 Zhiping Ye ^{a, d}, Yang Liu ^a, Anton Nikiforov ^b, Jiayu Ji ^a, Bo Zhao ^{c, *}, Jiade Wang ^{a, *}

4 ^a College of Environment, Zhejiang University of Technology, 18 Chaowang RD, Hangzhou
5 310014, PR China

6 ^b Ghent University, Faculty of Engineering, Department of Applied Physics, Research Unit Plasma
7 Technology, Sint-Pietersnieuwstraat 41, 9000 Ghent, Belgium

8 ^c Zhejiang Tuna Environmental Science & Technology Co., Ltd, Shaoxing 312071, PR China

9 ^d State Environmental Protection Key Laboratory of Sources and Control of Air Pollution Complex,
10 Beijing, 100084, China

11 **ABSTRACT**

12 A series of CeO₂-MnO_x for highly efficient catalytical oxidation of carbon monoxide were prepared
13 by citrate sol-gel (C), hydrothermal (H) and hydrothermal-citrate complexation (CH) methods. The
14 outcome indicates that the catalyst generated using the CH technique (CH-1:8) demonstrated the greatest
15 catalytic performance for CO oxidation with a T₅₀ of 98 °C, and also good stability in 1400 min.
16 Compared to the catalysts prepared by C and H method, CH-1:8 has the highest specific surface of 156.1
17 m²·g⁻¹, and the better reducibility of CH-1:8 was also observed in CO-TPR. It is also observed the high
18 ratio of adsorbed oxygen/lattice oxygen (1.5) in the XPS result. Moreover, characterizations by the TOF-
19 SIMS method indicated that obtained catalyst CH-Ce/Mn=1:8 had stronger interactions between Ce and
20 Mn oxides, and the redox cycle of Mn³⁺+Ce⁴⁺ ↔ Mn⁴⁺+Ce³⁺ was a key process for CO adsorption and
21 oxidation process. According to in-situ FTIR, the possible reaction pathway for CO was deduced in three
22 ways. CO directly oxidize with O₂ to CO₂, CO adsorbed on Mn⁴⁺ and Ce³⁺ reacts with O to form

23 intermediates (COO^-) ($T > 50\text{ }^\circ\text{C}$) and carbonates ($T > 90\text{ }^\circ\text{C}$), which are further oxidized into CO_2 .

24 **Keywords:** hydrothermal-citrate complexation (CH), CO oxidation, Ce-Mn redox cycle, In-situ
25 characterization

26 1. Introduction

27 The iron and steel industry (ISI) is a pillar industry of China's economy, accounting for 56.76% of
28 the global crude steel output in 2020 (Zhu et al., 2022). The air pollution emissions of ISI, especially CO
29 concentration in 1-2 orders of magnitude higher than other pollutants. It poses a major risk to both the
30 environment and public health (Ye et al., 2022; Yu et al., 2021). The catalytic oxidation of CO is regarded
31 as one of the finest methods for reducing the impact of ISI pollution not only in China but also on a
32 global scale.

33 Among different catalysts, Mn-based materials have been widely applied for CO removal due to the
34 ability of crystalline lattices to store oxygen and the high mobility of lattice oxygen (Gao et al., 2021;
35 Niu and Lei, 2019). The bimetallic catalysts can further strengthen the redox properties of the surface of
36 Mn-based materials. The kinetic study for CO oxidation performed over Cu-Ce catalysts shows that the
37 partial pressure dependence is 0-1 for CO and 0 for O_2 . This could be well interpreted by a Mars-
38 vanKrevelen type mechanism over these catalysts. (Jia et al., 2012) The DFT calculation results further
39 verify that the oxygen vacancies make the required reaction energy lower than the conventional reaction
40 method during the CO oxidation process.(Wang et al., 2022) The kinetics of CO oxidation on MnCeO_x
41 catalyst shows that the surface oxygen vacancies promote CO oxidation, special attention was paid to the
42 oxide structure leading to the most active catalyst. (Arena et al., 2017) The addition of the Ce element is
43 of great potential to change the crystal structure and valence state of MnO_x , and the substitution of Ce to
44 Mn helps to enhance the lattice oxygen activity, promoting the reactivity of CO oxidation reactions (Wei

45 et al., 2021).

46 The rise in ceria concentration of Ce-Mn oxides has also been reported to have different morphology
47 and microstructure: the nanorod particles became notably shorter and thinner, and some thick flakes or
48 agglomerates of shapeless nanoparticles were also seen, changing the mesopore properties and specific
49 surface area (Kharlamova et al., 2022). The Ce-Mn-O solid solution with superior catalytic activity was
50 made using a deposition coprecipitation technique. It has good stability during catalytical processes, and
51 CO oxidation for three successive runs was explored (Venkataswamy et al., 2015). Reports stated that
52 the E_a (activation energy) value of Mn-Ce solid solution for CO oxidation was about 30-40 $\text{kJ}\cdot\text{mol}^{-1}$
53 lower than that of manganese oxide and manganese-cerium oxide catalysts, suggesting the high reactivity of
54 Mn-Ce solid solution (Zhang et al., 2016).

55 Ce-Mn oxides have been reported to be available in a variety of forms due to their good
56 compatibility, and the solid solution is one of the most efficient structures due to the dispersity,
57 crystallinity, and anti-agglomeration (Lei et al., 2021; Zhang et al., 2021). Several routes have been
58 suggested for the preparation of Ce-Mn solid solution, such as impregnation (Yang et al., 2020), sol-gel
59 (Huang et al., 2019), coprecipitation (Tang et al., 2020), hydrothermal (Huang et al., 2021), and ion
60 exchange (Ji et al., 2021). The various preparation techniques affect the solid solution formation,
61 exhibiting different catalytic oxidation performances. However, the available research results can not
62 draw unambiguous conclusions on the method's selectivity and the relationship between it and solid
63 solution structure. Therefore, it is still worth putting more effort into detailed research of the effects.

64 In this work, the citric acid sol-gel, the hydrothermal, and citrate-hydrothermal methods were used
65 to prepare Mn-Ce solid solution. Considering the three carboxyl groups of citric acid, it is beneficial for
66 the complexation reaction between the carboxyl group and metal. The obtained precursors have a three-

67 dimensional network structure, which improves the dispersibility of the catalyst (Zhao et al., 2016). The
68 citric acid-hydrothermal coupling method has strong innovation and feasibility, as it can simultaneously
69 possess the high dispersion of the citric acid method and the high activity and stability of the
70 hydrothermal method to obtain more bimetallic active sites. The focus was put on how various
71 approaches affected the physicochemical properties of solid solutions, for instance, phase composition,
72 morphology, surface properties, and the efficiency of the CO oxidation over the Ce-Mn solid solution
73 structure. And the adsorption and oxidation of CO process were intensively studied. Hence, the link with
74 the preparation method and characteristics of $\text{CeO}_2\text{-MnO}_x$ was investigated using XPS, FE-SEM, TEM,
75 XRD, Raman spectrum, BET, CO-TPR, and H_2 -TPR. Furthermore, in situ DRIFTS, XPS, and TOF-
76 SIMS were used to explore a CO oxidation mechanism on $\text{CeO}_2\text{-MnO}_x$.

77 **2. Experimental set-up and methodology**

78 2.1. Catalysts preparation

79 The citric acid sol-gel process was used to create the catalysts designated as C-1:8. With a molar
80 ratio of 1:8, the necessary quantity of $\text{Ce}(\text{NO}_3)_3 \cdot 6\text{H}_2\text{O}$ and $\text{Mn}(\text{NO}_3)_2 \cdot 4\text{H}_2\text{O}$ was dissolved in 2 M citric
81 acid. The resulting solutions were heated to 70 °C and agitated for three hours before being dried in a
82 rotary evaporator. The resultant materials were dried for an additional day at 110 °C and calcined for
83 three hours at 500 °C.

84 The catalyst was made by the hydrothermal method named H-1:8. Both $\text{Ce}(\text{NO}_3)_3 \cdot 6\text{H}_2\text{O}$ and
85 $\text{Mn}(\text{NO}_3)_2 \cdot 4\text{H}_2\text{O}$ were dissolved in 20 mL of water at the same molar ratio of 1:8. To the mixture of Ce
86 and Mn precursors, 60 mL of 4 M NaOH was added dropwise and stirred for 30 min. The solution was
87 placed in a 100 mL autoclave at 100 °C for 24 h. The slurry samples were washed with deionized water,
88 dried at 60 °C, and calcined in air for 2 h.

89 Finally, the sample labelled as CH-1:8 was prepared using the citrate-hydrothermal (CH) method.
90 $\text{Mn}(\text{NO}_3)_2 \cdot 4\text{H}_2\text{O}$, citric acid, urea and $\text{Ce}(\text{NO}_3)_3 \cdot 6\text{H}_2\text{O}$, all at a concentration of 3 M, were added to the
91 beaker and mixed in the molar ratio of [urea]:[citric acid]:[Mn]:[Ce]=1.5:1.5:0.87:0.33, 0.3 M of KMnO_4
92 solution was then added dropwise. $[\text{Mn}(\text{NO}_3)_2]:[\text{KMnO}_4]$ in a molar ratio of 1:2. Subsequently, the
93 premixed solution was given a dropwise addition of 10 mL of ammonia solution (25wt%) until the pH
94 was 6-7. Four hours of mixing later, the combined liquid was loaded into a 100 mL hydrothermal kettle,
95 and the reaction was continued for 12 h at 180 °C. The slurry samples were then rinsed with deionized
96 water until the pH of the solution approached 7, dried at 80 °C for 12 h and calcined in air at 350 °C for
97 4 h.

98 2.2. Catalyst characterization

99 Using Cu K α radiation (= 0.1541 nm) and a PANalytical Empyrean powder diffractometer, the X-
100 ray diffraction (XRD) patterns were collected. The patterns were gathered using a 2 θ range with steps of
101 0.0167° between 10° and 80°. Herein, the average CeO_2 (110) particle size is computed by the Scherrer
102 formula: $L_a = k\lambda/\beta\cos\theta$, where k: Scherrer constant 0.89; β : the FWHM (full width at half maximum)
103 corresponding to the 110 peaks; λ : wavelength of X-ray ($\lambda=0.15406$ nm); θ : diffraction angle for the
104 peaks belonging to the 110 peaks.

105 The shape and structure of the samples were examined using a transmission electron microscope
106 (TEM, JEOL JEM-2010F) and a field emission scanning electron microscope (FE-SEM, HITACHI
107 Regulus 8100) at acceleration voltages of 130 kV and 300 kV, respectively.

108 Elemental analysis of calcined solids for Ce and Mn was conducted using an Agilent 720ES
109 spectrometer with inductively coupled plasma emission spectroscopy (ICP-OES). Prior to analysis, the
110 catalysts were resolved in a concentrated mixture of hydrochloric acid and nitric acid.

111 Brunauer-Emmett-Teller (BET) specific surface area and porosity of the samples were measured on
112 a Nova2000e analyzer (Quantachrome, USA) by adsorption of N₂ at 77 K. The samples were off-gassed
113 in nitrogen at 200 °C for 10 h before starting the analysis. For the purpose of calculating the specific
114 surface area and pore size distribution, BET and BJH were selected.

115 X-ray photoelectron spectroscopy (XPS) was performed using monochromatic Al K α radiation
116 ($h\nu=1486.2$ eV) and a Thermo Scientific K-Alpha instrument sample chamber. Since the XPS peaks have
117 multiple components, the peaks were analyzed for mixed Gaussian (70%)/Lorentzian (30%) shapes using
118 CasaXPS analysis software. Using the 284.8 eV binding energy of amorphous carbon as a calibration
119 reference.

120 The Renishaw inVia instrument produced Raman spectra. The sample testing conditions were: room
121 temperature with a 17 mW diode-pumped solid-state laser set at a laser wavelength of 532 nm and a
122 scanning wavelength range of 50-4000 cm⁻¹.

123 An experiment with a temperature program was used to investigate the catalysts' redox properties.
124 The 30-40 mg samples were purged with He gas flow (50 mL·min⁻¹) for one hour, cooled to 50 °C, after
125 which it was heated from 25 to 300 °C at a rate of 5 °C·min⁻¹ using a 5% H₂/Ar gas mixture (50 mL·min⁻¹)
126 for drying pretreatment. After the baseline is stable, the sample starts to be analyzed in the reducing
127 atmosphere. A Quartz U-shaped microreactor-equipped MicroActive for AutoChem II 2920 Version
128 catalyst analyzer was used to carry out the H₂ temperature-programmed reduction studies. TCD is used
129 to identify the reducing gas after the sample was desorbed at 800 °C in a 10% H₂/Ar gas flow. On a
130 Microtrac BELCat II catalyst analyzer, experiments for CO temperature programming reduction were
131 carried out. The sample was heated at 10 °C·min⁻¹ at 50-800 °C in a 10% CO/He environment. The
132 reducing gas was detected by a gas quality using the (m/z) signals of CO (28) and CO₂ (44) at an MFC

133 total flow rate of 30.00 SCCM.

134 With the aid of a TOF-SIMS5 spectrometer (PHI nano TOF II Time-of-Flight SIMS) fitted with a
135 bismuth liquid metal ion gun (LMIG), both positive and negative were performed. A pulsed Bi^{3+} primary
136 ion beam (30 keV, 2 nA) rastered across an $80 \times 80 \mu\text{m}^2$ surface area was used to bombard the tabled
137 samples. The overall fluence is below 10^{12} ions/ cm^2 with a data capture time of 100 s, assuring static
138 circumstances. An electron flood cannon with a 20 eV pulse was used to correct for charge effects. At
139 $m/z = 140$ for Ce^+ , the mass resolution (m/m) was around 7000. The precise mass of the secondary ions,
140 further to the intensities required for the anticipated isotope pattern, allowed for their identification.

141 The oxidation pathway of CO on the Ce-Mn catalyst was analyzed using the in situ DRIFTS analysis
142 technique. The instruments are Thermo Fisher's Nicolet IS50 FTIR and Harrick in situ reaction chamber
143 (HVC-DRM). The scanning range of $4000\text{-}600 \text{ cm}^{-1}$ and a resolution of 8 cm^{-1} were used with an average
144 of over 128 scans. Prior to CO oxidation experiments, background spectra was captured at room
145 temperature under a flow of pure N_2 until spectra became stable. Then, the spectrum of the sample (40-
146 60 mesh) at the temperature range of $20\text{-}200 \text{ }^\circ\text{C}$ was recorded, and the gaseous CO was evacuated using
147 ultra-high purity air.

148 2.3. Catalytic activity evaluation

149 2.3.1. CO oxidation curve

150 The catalyst (250 mg, 40-60 mesh) was reacted in 8 mm quartz tubes for the catalytic activity
151 evaluation, which was done in a fixed bed reactor. A K-type thermocouple in the catalyst bed provided
152 a temperature of $40\text{-}240 \text{ }^\circ\text{C}$, which was used to test the catalytic activity. At a mass air rate of 30,000
153 $\text{mL} \cdot \text{g}^{-1} \text{ h}^{-1}$, a mass flow controller measured the CO content to be 1500 ppm. After the gas had settled for
154 30 minutes following entrance, the test was initiated.

155 The CO conversion (X_{CO}) efficiency was calculated:

$$156 \quad X_{CO}(\%) = \frac{[CO]_{in} - [CO]_{out}}{[CO]_{in}} * 100\%$$

157 Yield of CO_2 (X_{CO_2}):

$$158 \quad X_{CO_2} = \frac{[CO_2]_{out}}{[CO]_{in}} * 100\%$$

159 where $[CO]_{out}$, $[CO_2]_{out}$ and $[CO]_{in}$ in represent the corresponding output and inlet is the outlet and
160 inlet concentrations of CO and CO_2 .

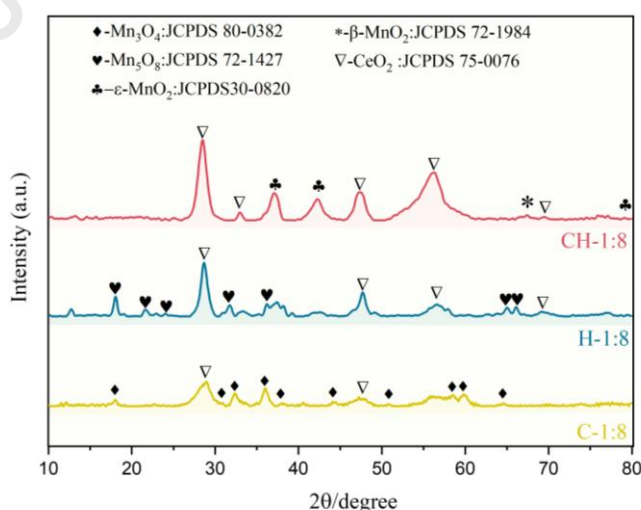
161 2.3.2. Stability test

162 Before the stability test, the samples were treated with airflow ($100 \text{ mL} \cdot \text{min}^{-1}$) at the temperature of
163 calcination for 1.5 h ($1^\circ \text{C} \cdot \text{min}^{-1}$). The stability experiment was performed at 110°C for 1440 min, and
164 the catalytic stability of the Ce-Mn samples was examined by gas chromatography with continuous
165 injection.

166 3. Results and Discussion

167 3.1. Catalyst characterization

168 3.1.1. Morphology and phase structures

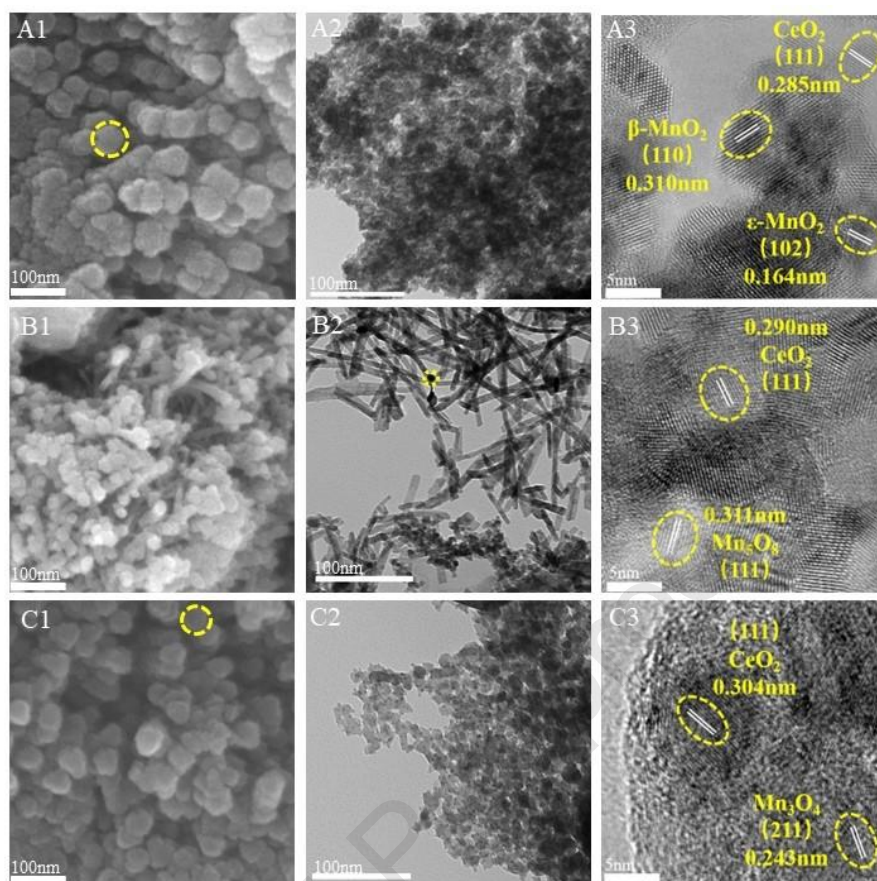


169

170 Fig. 1 displays the XRD patterns of the CH-1:8, H-1:8, and C-1:8 samples.

171 The phase compositions of all catalysts were analysed by X-ray diffraction, and the corresponding
172 diffraction patterns are collected in Fig. 1. The fluorite structure of the CeO₂ phase was observed clearly
173 in all three samples. For CH-1:8, the diffraction peaks at $2\theta = 37.12^\circ$, 42.40° , and 78.92° correspond to
174 ϵ -MnO₂ (JCPDS30-0820). The peaks with 2θ values of 28.75° , 56.82° , and 67.44° attributed to β -MnO₂
175 (JCPDS 72-1984). The diffraction peaks of Mn₅O₈ (JCPDS 72-1427) were observed for the H-1:8 sample.
176 As can be observed, the C-1:8 diffraction peaks were accurately identified as Mn₃O₄ (JCPDS 80-0382).
177 Meanwhile, the diffraction peaks of all the CeO₂-MnO_x catalysts exhibit a minor shift when compared
178 to pure CeO₂, and comparable outcomes were also reported (Zhu et al., 2017). The reason for this
179 phenomenon may be the entry of Mn ions into the CeO₂ lattice to create CeO₂-MnO_x solid solution.
180 Referring to the Hume-Rothery criterion in SI (Otto et al., 2013), empirical values are obtained: when
181 $\Delta R/R$ (relative difference of radii R) is lower than 30%, solid solutions can be formed, and the $\Delta R/R$ of
182 Ce-Mn material is 22.9%, so it is possible to form a solid solution.

183 Furthermore, the crystallite sizes of the Ce-Mn samples were estimated using the Scherrer equation
184 from the broadening of the CeO₂ (111) facet diffraction peak at $2\theta=28.5^\circ$. As displayed in Table S1, the
185 crystallite size of the CH-1:8, C-1:8, and H-1:8 samples is 9.18 nm, 7.56 nm, and 10.45 nm, respectively.



186

187 **Fig. 2.** FE-SEM images of various CeO₂-MnO_x samples of CH-1:8(A1), H-1:8(B1), C-1:8(C1) catalysts;

188

TEM images of CH-1:8(A2-3), H-1:8(B2-3), C-1:8(C2-3) catalysts.

189

FE-SEM and TEM were used to examine the morphologies of catalysts. CH-1:8 and C-1:8 both

190

show a similar nanosphere, and CH-1:8 has an average particle size of 48.2 nm., while that of C-1:8 is

191

45.5 nm. According to the mapping in fig. S1, H-1:8 is composed of rod-shaped CeO₂ and part of the

192

MnO_x spherical small particles, the diameters of the nanorods and spheres are around 8.7 nm and 8.0 nm,

193

respectively. To further reveal the materials' morphology and crystal structure, TEM characterization

194

was performed. Fig. 2(C1) is the HRTEM image of the H-1:8 catalyst, the (110) plane of β-MnO₂ (JCPDS

195

72-1984) is responsible for the 0.310 nm lattice fringes. The (102) plane of ε-MnO₂ (JCPDS 30-0820)

196

can be used to identify the 0.164 nm lattice fringes. The lattice striations of Mn₅O₈ and Mn₃O₄ can also

197

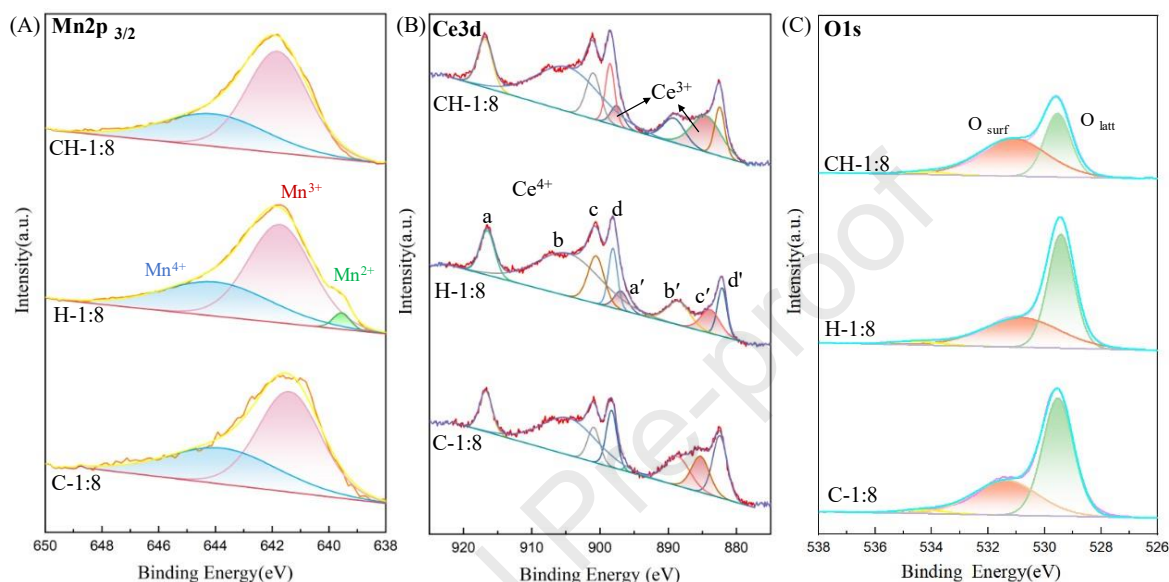
be seen in Fig. 2(C2) and Fig. 2(C3), respectively. The (111) plane of pure CeO₂ is responsible for the

198 0.311 nm lattice fringes. According to the standard card (JCPDS 75-0076). In the CeO₂-MnO_x samples,
199 the (111) face spacing of the composite catalysts were reduced compared to the pure CeO₂, CH-1:8, H-
200 1:8, and C-1:8 was reduced to 0.285 nm, 0.307 nm, and 0.304 nm, respectively. The inclusion of Mn
201 may deform the CeO₂ lattice leading to the lattice edges of Ce shrinking (Wang et al., 2017), considering
202 the radius of Mn³⁺ (0.058 nm) and Mn⁴⁺ (0.053 nm) have substantially lower than Ce³⁺ (0.103 nm) and
203 Ce⁴⁺ (0.087 nm), making it easier for incorporation of Mn into Ce lattice. This is corroborated by the
204 slight shift in the position of the CeO₂ (111) peak in the XRD result. It has been shown that the β-MnO₂
205 (110) crystal plane has the characteristics of the most stable and preferential exposure (Lin et al., 2021).

206 Nitrogen sorption measurements at 77 K were used to evaluate the porosity of the samples. Figure
207 S2 shows the N₂ adsorption-desorption isotherms for CH-1:8, H-1:8, and C-1:8. The catalysts' N₂
208 adsorption-desorption isotherms are comparable, as seen in Fig. S2, demonstrating the properties of
209 mesoporous materials. Table S1 displays the precise surface areas, typical pore sizes, and volumes. The
210 CH-1:8, H-1:8, and C-1:8 catalysts have specific surface areas of 156.1, 77.3, and 35.1 m²·g⁻¹,
211 respectively. The increased surface area helps the CO oxidation rate to rise. According to Fig. S1, we
212 can find that the CH-1:8 showed significantly higher N₂ adsorption than the other two catalysts at p/p₀
213 less than 0.1. The microporous pore volumes of CH-1:8 (0.0218 cm³·g⁻¹) is much larger than H-
214 1:8(0.0159 cm³·g⁻¹) and C-1:8 (0.0021 cm³·g⁻¹).

215 3.1.2. The elemental analysis

216 ICP-OES analysis in Table S2 confirms the element component of bulk samples. The Ce/Mn atomic
 217 ratios of CH-1:8, H-1:8, and C-1:8 is 1:6.5, 1:8.8, and 1:4.2, respectively. Considering the atomic ratios
 218 of XPS spectra, it is observed higher dispersion of cerium oxides than manganese oxides on the surface.



219 **Fig. 3.** XPS spectra of (A) Mn 2p, (B) Ce 3d and (C) O1s for CeO₂-MnO_x catalysts.

220 The surface elements of the CeO₂-MnO_x catalyst were characterised by XPS. The resulting XPS
 221 spectral data are shown in Figure 3, and the corresponding quantitative results are listed in Table S2. In
 222 Fig.3(A), the Mn 2p XPS envelope of H-1:8 was deconvoluted to three major characteristic peaks at
 223 639.5 eV, 641.7 eV, and 643.9 eV, which are indicative of Mn²⁺, Mn³⁺, Mn⁴⁺ (Zhao et al., 2019).
 224 Conversely, the citrate-related methods exhibited two curve-fitting peaks with BE of 644.1 (± 0.3) eV
 225 and 641.8 (± 0.4) eV for Mn³⁺ and Mn⁴⁺, respectively. Integration of the peaks leads to Mn³⁺/Mn⁴⁺ atomic
 226 ratio closing to 1.85 (CH-1:8), 1.69 (H-1:8), and 1.59 (C-1:8), as shown in Table S2. Considering the
 227 electrostatic balance, the quantity of oxygen vacancies had a similar pattern. The XPS Mn AOS of CH-
 228 1:8, H-1:8, and C-1:8 is 3.23, 3.45, and 3.56. It revealed that Mn³⁺ is the dominant oxidation state for
 229 CH-1:8 and H-1:8, in comparison with Mn⁴⁺ for C-1:8.

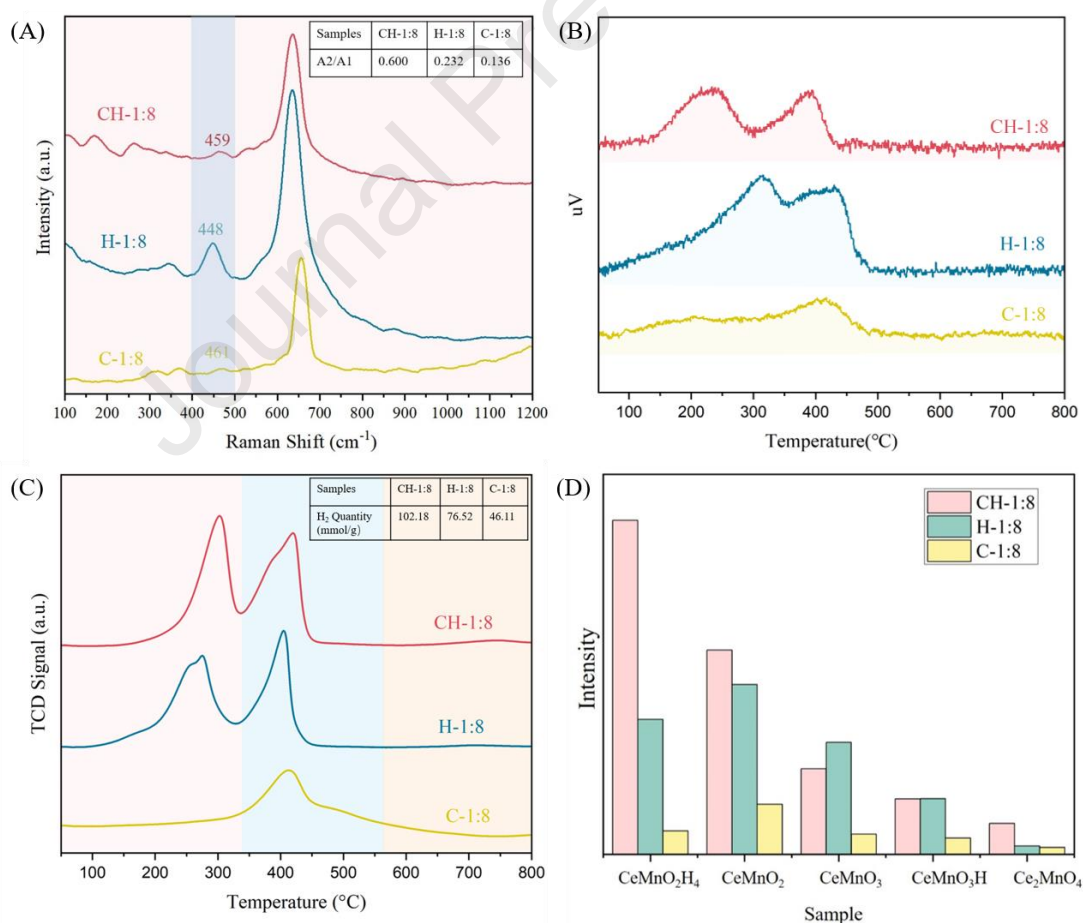
230 The Ce 3d spectra of the ready-made samples are given in Fig. 3. (B). The split-orbit multiplex lines
231 of the $3d_{3/2}$ and $3d_{5/2}$ signals, which may be divided into m and n series, were deconvoluted into eight
232 distinctive peaks. Among these characteristic peaks, a (916.7 ± 0.2 eV), b (904.7 ± 0.1 eV), c (900.8 ± 0.2
233 eV), and d (898.5 ± 0.2 eV) were assignable to Ce^{4+} $3d_{3/2}$ lines, while b' (889.2 ± 0.2 eV) and d' ($882.4 \pm$
234 0.2 eV) can be attributable to Ce^{4+} $3d_{5/2}$ lines. While, a' at 897.5 ± 0.2 eV ($3d_{5/2}$) and c' at 884.4 ± 0.3 eV
235 ($3d_{5/2}$) were assignable to Ce^{3+} (Yang et al., 2019). Using multi-peak fitting, the molar ratio of Ce^{3+} to
236 Ce^{4+} was obtained, exhibiting the order of CH-1:8 (0.23) > H-1:8 (0.12) > C-1:8 (0.13) in Table S2. CH-
237 1:8 prepared still shows a high amount of low-valent Ce^{3+} and Mn^{3+} , pointing to a significant number of
238 oxygen vacancies. (Wan et al., 2022).

239 The O1s spectra shown in Fig. 3(C) are separated into two peaks at 529.3 eV and 531.3 eV for
240 lattice oxygen (O_{latt}) and surface active oxygen (O_{surf}) (Liao et al., 2022). The atomic ratio of O_{surf}/O_{latt} is
241 generally used to analyze the creation of surface oxygen vacancies resulting in the formation of oxygen-
242 adsorbed species, which is an important parameter related to catalytic redox ability. The CH-1:8 sample
243 has the highest ratio of O_{surf}/O_{latt} (1.5) compared to H-1:8 (0.6) and C-1:8 (0.9).

244 3.1.3. Raman

245 The structures of CH-1:8, H-1:8, and C-1:8 catalysts were further characterized by Raman
246 spectroscopy in Fig. 4(A). The Raman spectra of all CeO_2 - MnO_x catalysts showed a peak at 445-465 cm^{-1}
247 ¹ that shifted to a lower wavelength compared with the F2g band of the pure CeO_2 at 464 cm^{-1} . It was
248 explained by the deformation of the CeO_2 lattice and the phonon effect in the generation of the Ce-Mn
249 solid solutions, resulting in the generation of oxygen vacancies (Luo et al., 2020). The distortion of Ce-
250 O bonding symmetry was also observed using TEM. The catalyst exhibits principal Raman bands at 463
251 cm^{-1} and 600 cm^{-1} for the cubic fluorite structure with F2g vibrations (labelled 1) and defect-induced

252 modes (D band, labelled 2). The D band is associated with oxygen vacancies in the cerium-based material,
 253 and the intensity ratio of F2g to D (A2/A1) reflects the proportional correlations to the amount of the
 254 surface-level vacancy of oxygen (Yao et al., 2017). The table in Fig. 4(C) includes a summary of the
 255 findings. That indicates A2/A1 for CH-1:8 is 0.6, which is significantly larger than that for H-1:8 (0.232)
 256 and C-1:8 (0.136). In addition, the $\text{CeO}_2\text{-MnO}_x$ catalysts show a clear Raman peak placed at 635-651
 257 cm^{-1} and an unremarkable peak at 500-510 cm^{-1} , which were assigned to the Mn-O-Mn and Mn-O
 258 stretching structures, respectively (Ma et al., 2022; Venkataswamy et al., 2015). And the $\beta\text{-MnO}_2$
 259 characteristic peaks of CH-1:8 were also observed at 187, 584, and 635 cm^{-1} , which was in agreement
 260 with the XRD pattern.



261

262 **Fig. 4.** (A) Raman spectra, (B) CO-TPR curves, (C) H_2 -TPR curves, and (D) $\text{Ce}_x\text{Mn}_y\text{O}_z\text{H}_w$ secondary ions (+) and

263

(-) fragments of the synthesized catalysts (CH-1:8, H-1:8, C-1:8).

264 3.1.4. CO-TPR and H₂-TPR

265 CO-TPR and H₂-TPR were used to investigate the redox properties of Ce and Mn species. the
266 corresponding CO consumption measured online during this experiment is shown in Fig. 4(B). At 150-
267 350 °C and 300-500 °C, the catalysts as-prepared exhibit two increased reduction peaks. While it is
268 observed the weak peak of C-1:8 at low temperatures among samples. Considering the reducibility
269 enhancement effect by the incorporation of Ce to Mn, the first reduced peak is believed to be the mixture
270 reduction of Ce⁴⁺ to Ce³⁺ and MnO₂ to Mn₃O₄ in the catalyst, and the following peak is responsible for
271 converting Mn₃O₄ into MnO stage (Chen et al., 2019). It is noted that a rapid CO consumption is observed
272 at 100-200 °C, suggesting the excellent CO oxidation ability of CH-1:8 compared to the other two
273 catalysts.

274 It is interesting to find the similar characteristic peaks of CO-TPR and H₂-TPR figures of prepared
275 catalysts, except for the C-1:8 sample (Fig. 4(B-C)). The consumption of H₂ showed 102.18 mmol·g⁻¹
276 (CH-1:8), 76.52 mmol·g⁻¹ (H-1:8), and 46.11 mmol·g⁻¹ (C-1:8). And the peak position of CO-TPR at
277 409.6 °C (C-1:8) > 319.2 °C (H-1:8) > 242.4 °C (CH-1:8). For the CH-1:8 sample, it is also observed
278 that the low temperature reduction peaks had shifted to the left and that the second peak of the CO-TPR
279 profile had widened in the comparison of H₂-TPR, suggesting the higher mobility and accessibility of
280 CO than H₂ through the CH-1:8 surface (Sacco et al., 2022).

281 3.1.5. TOF-SIMS

282 TOF-SIMS was used to explore the top layer (1-3 nm) of the CH-1:8, H-1:8, and C-1:8 catalysts,
283 analyzing the chemical compositions. It should be noted that the detection of polar Ce_xMn_yO_zH_w
284 secondary ions (+) and (-) has been compiled in Table S3 and Fig. 4(D). The data exhibits the presence
285 of CeMnO₂, CeMnO₃H, Ce₂MnO₄, CeMnO₃, and CeMnO₂H₄ fragments, indicating the formation of the

286 Ce-Mn intermetallic species on the catalyst surface. The detection of a large number of secondary ions
287 shows that the mixing of Mn, Ce, and O leads to the composition of homogeneous nanoscale materials,
288 which is consistent with the TEM characterization result that Mn enters into the CeO₂ lattice to form Ce-
289 Mn solid solution. Concurrently, the results of TOF-SIMS measurements clearly proved that the total
290 relative polar strengths of Ce-Mn intermetallic species contained in the CH-1:8 sample (0.431%) are
291 clearly stronger than that of H-1:8 (0.3%) and C-1:8 samples (0.178%).

292 3.2. Catalytic performance

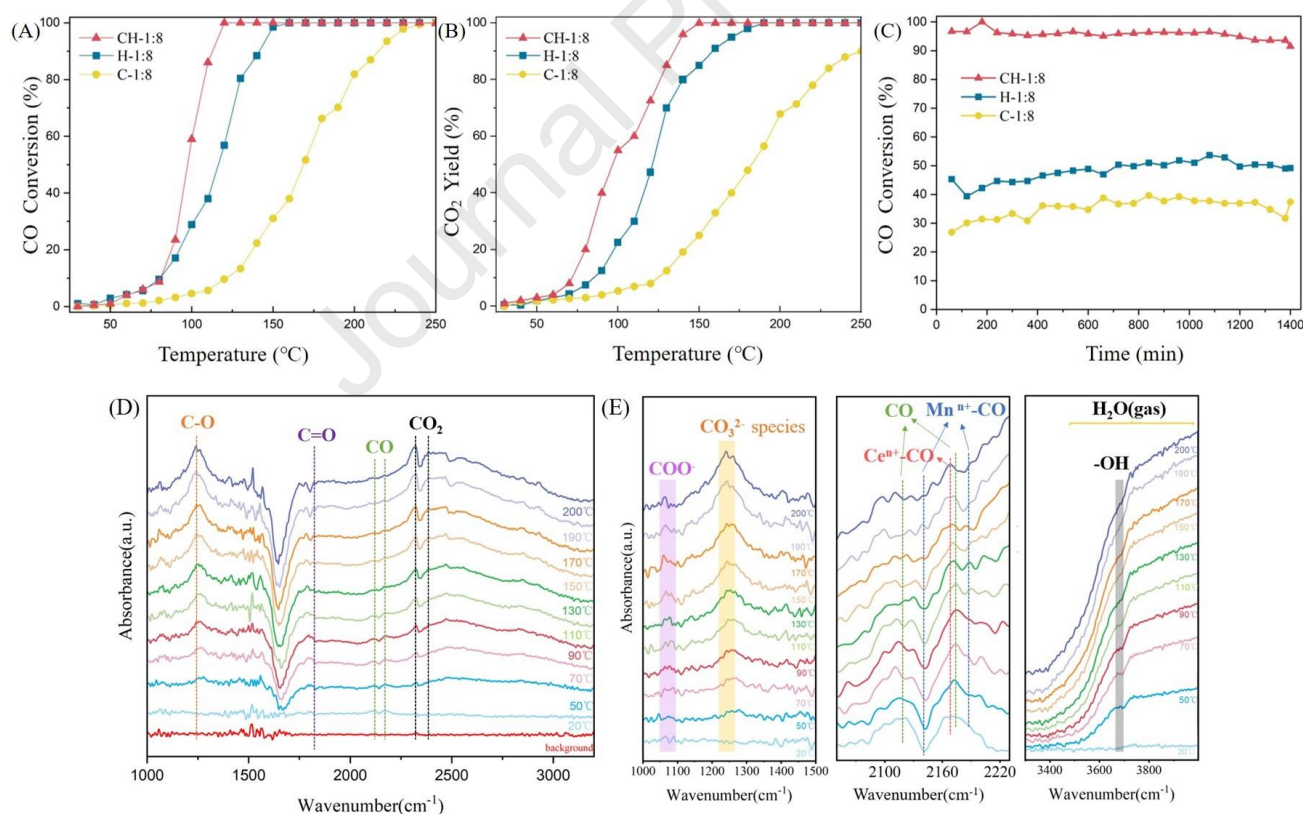
293 The findings of the evaluation of the CeO₂-MnO_x samples' catalytic abilities for CO oxidation are
294 displayed in Fig. 5. Fig. 5(A) demonstrates that the CH-1:8 has the best CO conversion, and the T₉₀ is
295 maintained at 110 °C, followed by H-1:8 (T₉₀=142 °C) and C-1:8 (T₉₀=205 °C), and the CO₂ yield was
296 also showed the same trend by CH-1:8 (T₉₀=128 °C), H-1:8 (T₉₀=156 °C) and C-1:8 (T₉₀=225 °C). On
297 the other hand, T₅₀ and T₉₀ values of CH-1:8 are smaller than most other Ce-Mn-based catalysts,
298 indicating that it is highly competitive, as shown in Table S4. For comparison, the CO reaction rate was
299 calculated due to the different reaction conditions. The reaction rate of CO on CH-1:8 is also faster than
300 the reaction rate of most of the other catalysts. In fact, the reaction rate of CH-1:8 at 115 °C is 2.36E-07
301 molCO·g⁻¹·s⁻¹, which is much higher than those of H-1:8 (1.18E-07 mol molCO·g⁻¹·s⁻¹) and C-1:8
302 (2.36E-08 molCO·g⁻¹·s⁻¹)

303 In addition, the stability of 1440 min tests have been performed at 115 °C over three CeO₂-MnO_x
304 catalysts, and Fig. 5(C) shows the conversion of CO to CO₂ with respect to time. For all samples, there
305 was no discernible difference in the effectiveness of CO removal, suggesting that the catalyst has good
306 stability. The citric acid acts as a chelating and reducing agent in the preparation process, which results
307 in an increase in the specific surface area and the Ce³⁺/Ce⁴⁺ ratio.

308 3.3. CO catalytic mechanism

309 To further investigate the CO oxidation process over CH-1:8, the DRIFTS and XPS were carried
 310 out. According to Fig. 5(D), the bands centring at 2360 cm^{-1} and 2341 cm^{-1} related to gaseous CO are
 311 identified at ambient temperature in the DRIFTS spectra collected between $20\text{ }^{\circ}\text{C}$ and $200\text{ }^{\circ}\text{C}$. At $70\text{ }^{\circ}\text{C}$,
 312 gradually lowering the distinctive CO peaks, the emergence of the CO_2 peak at 2359 cm^{-1} and 2338 cm^{-1}
 313 $^{-1}$ followed, indicating the occurrence of CO oxidation. The antisymmetric stretch of C-O and C=O,
 314 respectively, is largely attributed to the two additional peaks at 2359 cm^{-1} and 2338 cm^{-1} . Fig. 5(E)

315 **Fig. 5.** CO conversion (A), CO_2 yield (B), and stability tests at 115°C (C) of CH-1:8, H-1:8, and C-1:8
 316 catalysts (1500 ppm of CO, 30000 h^{-1}). DRIFTS spectra of CO oxidation on CH-1:8 catalyst among 1000-3200
 317 cm^{-1} (D), 1000-1500 cm^{-1} , 2050-2230 cm^{-1} , and 3300-4000 cm^{-1} (E).



318 demonstrates, the characteristic peak at $1060\text{-}1076\text{ cm}^{-1}$ and $1230\text{-}1260\text{ cm}^{-1}$ originate from the
 319 carboxylate ($T > 50\text{ }^{\circ}\text{C}$) and carbonate species ($T > 90\text{ }^{\circ}\text{C}$). The peak at $3500\text{-}3950\text{ cm}^{-1}$ represents the

320 production of $\text{H}_2\text{O}_{(\text{gas})}$, rising with the temperature. The OH^- of the metal surface is responsible for the
321 peak at $3650\text{-}3700\text{ cm}^{-1}$, and it decreases owing to the rise in temperature. At 2170 cm^{-1} after $150\text{ }^\circ\text{C}$, a
322 peak for CO linear adsorbed on $\text{Ce}^{\text{n+}}$ was found, and the peak's strength grew in step with the rising
323 temperature. It should be observed that the intensity in the $\text{Mn}^{\text{n+}}\text{-CO}$ band (2138 cm^{-1} and 2188 cm^{-1})
324 increases with rising temperature on account of improved relation between $\text{Mn}^{\text{n+}}$ active sites and CO
325 molecules adsorbed on them, reaching its peak at $130\text{ }^\circ\text{C}$.

326 From the XPS results (Table S2), it is clear that the ratio of $\text{O}_{\text{surf}}/\text{O}_{\text{latt}}$ is greatly reduced after CO
327 oxidation, demonstrating that this reaction covered the surface oxygen on the catalyst. (Eq. D.1). Raman
328 spectroscopy also shows the existence of the oxygen vacancy on the catalyst's surface, which could be
329 advantageous for the adsorption of the reactants. Hence, it is believed that $\text{CO}_{(\text{ads})}$ reacts with the
330 surrounding adsorbed oxygen to generate CO_2 (route 1). Compared to the adsorption energies obtained
331 for CO on $\beta\text{-MnO}_2$ (1 1 0) facet ($45.37\text{ kJ}\cdot\text{mol}^{-1}$) and pure CeO_2 ($60.68\text{ kJ}\cdot\text{mol}^{-1}$), CO is more likely to
332 be adsorbed at $\beta\text{-MnO}_2$ (1 1 0) site, which is in good agreement with DRIFT data, Mn-CO appeared at a
333 lower temperature than Ce-CO (Fig. 5(E)). On the other hand, the oxidation of CO takes place with the
334 involvement of not only the surface-adsorbed oxygen species but also the surface lattice oxygen (Eq B.1-
335 B.4). Polychronopoulou et al employed $^{18}\text{O}/^{16}\text{O}$ isothermal isotope exchange to show that lattice
336 oxygen in cerium oxide is involved in the synthesis of CO_2 from CO-s or $\text{CO}_{(\text{g})}$ (Polychronopoulou et
337 al., 2021). Ce-Mn followed the Mv-K mechanism, in which the CO adsorbed on Mn sites shown in
338 Process 4 in Fig. 6 could react with lattice oxygen from Mn-O-Mn, Ce-O-Ce, and Mn-O-Ce. Mn^{4+} reacts
339 with CO to form Mn^{3+} (Eq. G.1-G.2), the XPS result also showed that the ratio of $\text{Mn}^{3+}/\text{Mn}^{4+}$ increased
340 from 1.85 to 2.31 after the CO reaction, a process that requires electrons. Meanwhile, the ratio of

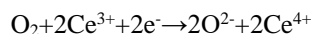
341 Ce^{3+}/Ce^{4+} decreased from 0.23 to 0.17, the valence state of Ce increasing, transferring electrons to Mn,
 342 thus forming a redox electron pair (Ce^{4+}/Ce^{3+} and Mn^{3+}/Mn^{4+}) (Eq. A.1-A.4).

343 As a particular number of OH groups on the catalyst surface in DRIFT as Fig. 5(E) shown, (route
 344 2) adsorbed CO on Mn^{4+} and Ce^{3+} forms the intermediate (COO^-)($T > 50$ °C) by a reaction with the
 345 nearby O from OH, which further oxidizes into CO_2 and H_2O in Fig. 6 (Eq. E.1-E.2). This is consistent
 346 with the results of increased COO^- and $H_2O_{(gas)}$ peak intensities and decreased metal-OH peak in DRIFT
 347 spectra. Furtherly gas phase O_2 supplemental oxygen vacancies to complete the catalytic cycle as process
 348 2 (Li et al., 2020).

349 **Table 1**

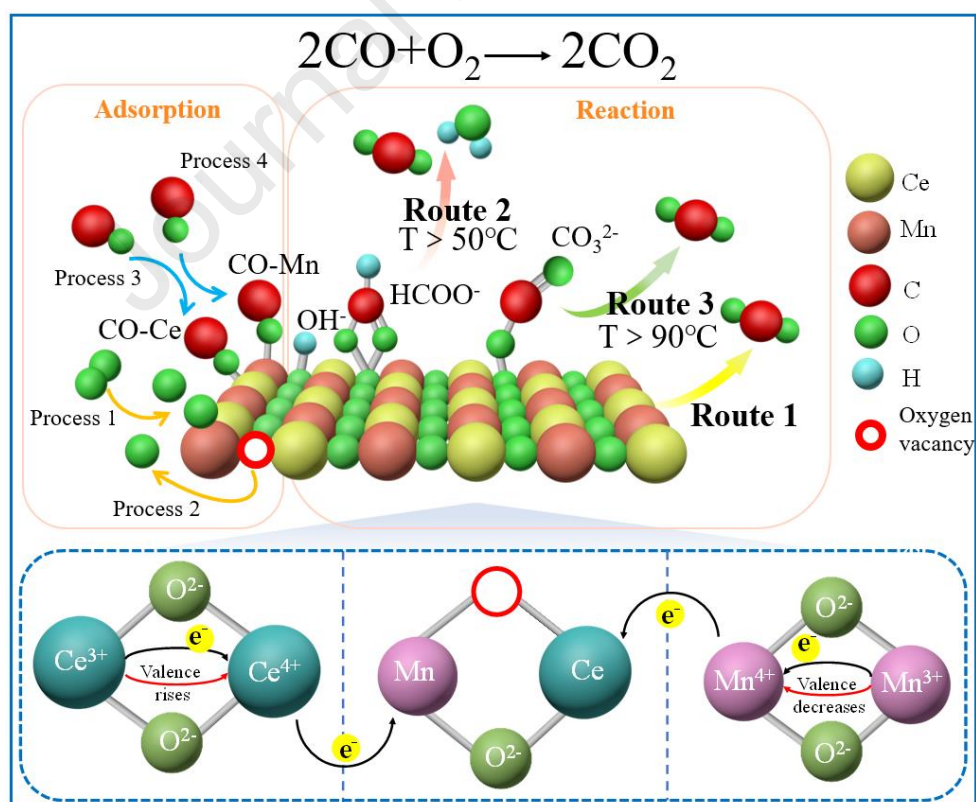
350 Potential processes in the catalytic oxidation of CO.

	CO oxidation process	
Electron transfer between Ce and Mn	$O^{2-} (latt) + Mn^{4+} \rightarrow O^- + Mn^{3+}$	Eq. A.1
	$O^{2-} (latt) + Ce^{4+} \rightarrow O^- + Ce^{3+}$	Eq. A.2
	$Mn^{3+} + Ce^{4+} \rightarrow Ce^{3+} + Mn^{4+}$	Eq. A.3
	$2Ce^{3+} + 1/2O_2(gas) + V_o \rightarrow 2Ce^{4+} + O^{2-}(ads) \rightarrow 2Ce^{4+} + O^{2-}(surf) \rightarrow 2Ce^{4+} + O^{2-}(latt) + V_o$	Eq. A.4
Adsorption migration of O_2	$O_2(gas) \rightarrow O_2(ads)$	Eq. B.1
	$O_2(ads) + 4e^- \rightarrow 2O^{2-}(ads)$	Eq. B.2
	$O^{2-}(ads) - e^- \rightarrow O^-(ads)$	Eq. B.3
	$O^{2-}(ads) \rightarrow O^{2-}(latt)$	Eq. B.4
Adsorption of CO	$CO(gas) \rightarrow CO(ads)$	Eq. C.1
Route 1	$CO(ads) + O^{2-} \rightarrow CO_2 + 2e^-$	Eq. D.1
Route 2	$CO(ads) + OH^-(surf) \rightarrow HCOO^-$	Eq. E.1
	$2HCOO^- + O^{2-} \rightarrow 2CO_2 + H_2O$	Eq. E.2
Route 3	$CO(ads) + 2O^{2-}(ads) \rightarrow CO_3^{2-} + 2e^-$	Eq. F.1
	$CO_3^{2-} + O^{2-} \rightarrow CO_2 + 2O^{2-}$	Eq. F.2
Total reaction	$CO(ads) + O^{2-}(ads) + 2Mn^{4+} \rightarrow CO_2 + 2Mn^{3+}$	Eq. G.1



Eq. G.2

351 Another parallel route is suggested that CO oxidation happens when carbonate ($T > 90^\circ\text{C}$) forms
 352 according to DRIFT in Fig. 5(E), (route 3). The oxygen vacancy in an O_2 atmosphere will initially be
 353 filled by dioxygen by its bonding to the Mn and Ce ions, creating two activated surface O. CO (ads) in
 354 combination with activated surface O form carbonate intermediates (CO_3^{2-}) as Fig. 5(E) shown the band
 355 attributed to carbonate species at $1230\text{-}1260\text{ cm}^{-1}$ rises with temperature but remains flat after 170°C ,
 356 indicating the decomposition of these carbonate substances into CO_2 . It has been reported that unidentate
 357 carbonate species are thermally more stable than inorganic carboxylate, and can be stable up to 200°C
 358 (Schweke et al., 2018). It is consistent with their function as important chemical intermediates in the
 359 catalytic CO oxidation cycle (Eq. F.1-F.2) because COO^- and CO_3^{2-} sites have IR bands for CO. It is
 360 worth noting that Mn-O and Ce-O often function as adsorption sites in the process.



361

362 **Fig. 6.** Mechanism of catalytic oxidation of CO on Ce-Mn catalyst: adsorption (Process 1-4), reaction

363

(Route 1-3), and the electron transfer in Ce-O-Mn.

364 4.Conclusions

365 In this experiment, Ce-Mn catalyst was used, and three methods were used to prepare the catalyst
366 by citrate-hydrothermal method, sol-gel method, and hydrothermal method. When the volumetric air
367 velocity is 30000 mL·min⁻¹ and the CO concentration is 1500 ppm, the catalytic oxidation efficiency can
368 reach T₉₀=115 °C, and it shows good stability after 1440 min of operation. It is possible to outline how
369 the preparation procedure affects the catalytic oxidation of CO at low temperatures:

370 (1) Smaller grain size and greater specific surface area are characteristics of the catalysts obtained
371 by the hydrothermally assisted sol-gel method; additionally, the increased Ce³⁺/Ce⁴⁺ ratio enables more
372 oxygen vacancies and unsaturated chemical bonds to be generated, which improves catalytic
373 performance.

374 (2) The cycles and reactions of Mn⁴⁺+Ce³⁺↔Mn³⁺+Ce⁴⁺ enhance the CO adsorption and oxidation
375 process. Individual electrons at the reaction interface and the manganese substitution in the catalyst
376 crystal are critical to the catalytic process.

377 (3) The catalytic oxidation of CO at the reaction interface of Ce-Mn bimetal follows the mechanism
378 of M-vK, CO molecules and lattice oxygen at the reaction interface the catalyst reacts with lattice oxygen
379 instead of gas-phase oxygen, and the CO oxidation cycle has three processes, the first process is CO
380 oxidation, then the surface re-oxidation and the third stage of CO oxidation. The reaction between lattice
381 oxygen and CO adsorbed on metal ions produces intermediates: COO⁻ and carbonates. Therefore, CO
382 oxidation efficiency is heavily reliant on the mobility and redox performance of oxygen in the catalyst.

383 (4) The catalyst preparation method in this work would be helpful to improve the preparation
384 method of other present catalysts. In addition, Ce-Mn exhibits comparable CO oxidation activity,

385 excellent redox properties, and greater specific surface area, indicating the application of a promising
386 non-noble metal catalyst in CO-containing flue gases.

387 **Acknowledgments**

388 This publication was funded by the National Natural Science Foundation of China (No.22108255),
389 China Postdoctoral Science Foundation (2022M712226), and the State Environmental Protection Key
390 Laboratory of Sources and Control of Air Pollution Complex (SCAPC202108). The TOF-SIMS study
391 was performed by Qiannan Ma of Shiyanjia laboratory (www.shiyanjia.com), for which the authors are
392 appreciative.

393 **References**

394 **Uncategorized References**

- 395 Arena F, et al., 2017. Probing the functionality of nanostructured MnCeO_x catalysts in the carbon
396 monoxide oxidation. *Applied Catalysis B: Environmental*; 210: 14-
397 22. <https://doi.org/10.1016/j.apcatb.2017.03.049>.
- 398 Chen J, et al., 2019. A facile strategy of enhancing interaction between cerium and manganese oxides for
399 catalytic removal of gaseous organic contaminants. *Applied Catalysis B: Environmental*; 250: 396-
400 407. <https://doi.org/10.1016/j.apcatb.2019.03.042>.
- 401 Gao Y, et al., 2021. Mechanisms and energetics of CO oxidation on MnO₂-supported Pt₁₃
402 clusters. *Applied Surface Science*; 560: 150017. <https://doi.org/10.1016/j.apsusc.2021.150017>.
- 403 Huang J, et al., 2019. The promotional role of Nd on Mn/TiO₂ catalyst for the low-temperature NH₃-SCR
404 of NO_x. *Catalysis Today*; 332: 49-58. <https://doi.org/10.1016/j.cattod.2018.07.031>.
- 405 Huang XS, et al., 2021. A strategy for constructing highly efficient yolk-shell Ce@Mn@TiO_x catalyst
406 with dual active sites for low-temperature selective catalytic reduction of NO with NH₃. *Chemical*
407 *Engineering Journal*; 419: 129572. <https://doi.org/10.1016/j.cej.2021.129572>.
- 408 Ji S, et al., 2021. Fabrication of a wide temperature Mn-Ce/TNU-9 catalyst with superior NH₃-SCR
409 activity and strong SO₂ and H₂O tolerance. *New Journal of Chemistry*; 45: 3857-
410 3865. <https://doi.org/10.1039/d0nj05404f>.

- 411 Jia A-P, et al., 2012.CO oxidation over $\text{CuO/Ce}_{1-x}\text{Cu}_x\text{O}_{2-\delta}$ and $\text{Ce}_{1-x}\text{Cu}_x\text{O}_{2-\delta}$ catalysts: Synergetic
412 effects and kinetic study.Journal of Catalysis; 289: 199-
413 209.<https://doi.org/10.1016/j.jcat.2012.02.010>.
- 414 Kharlamova TS, et al., 2022.Effect of metal-doping (Me = Fe, Ce, Sn) on phase composition, structural
415 peculiarities, and CO oxidation catalytic activity of cryptomelane- type MnO_2 .Journal of Alloys and
416 Compounds; 917: 17.<https://doi.org/10.1016/j.jallcom.2022.165504>.
- 417 Lei Z, et al., 2021.Study on denitration and sulfur removal performance of Mn-Ce supported fly ash
418 catalyst.Chemosphere; 270: 128646.<https://doi.org/10.1016/j.chemosphere.2020.128646>.
- 419 Li Z, et al., 2020.Oxygen vacancy mediated $\text{Cu}_y\text{Co}_3\text{-yFe}_1\text{O}_x$ mixed oxide as highly active and stable
420 toluene oxidation catalyst by multiple phase interfaces formation and metal doping effect.Applied
421 Catalysis B: Environmental; 269: 118827.<https://doi.org/10.1016/j.apcatb.2020.118827>.
- 422 Liao Y, et al., 2022.The Unique CO Activation Effects for Boosting NH_3 Selective Catalytic Oxidation
423 over $\text{CuO}_x\text{-CeO}_2$.Environ Sci Technol; 56: 10402-10411.<https://doi.org/10.1021/acs.est.2c02612>.
- 424 Lin F, et al., 2021.Investigation of chlorine-poisoning mechanism of $\text{MnO}_x/\text{TiO}_2$ and $\text{MnO}_x\text{-CeO}_2/\text{TiO}_2$
425 catalysts during o-DCB_z catalytic decomposition: Experiment and first-principles calculation.J
426 Environ Manage; 298: 113454.<https://doi.org/10.1016/j.jenvman.2021.113454>.
- 427 Luo Y, et al., 2020. MnO_2 nanoparticles encapsulated in spheres of Ce-Mn solid solution: Efficient catalyst
428 and good water tolerance for low-temperature toluene oxidation.Applied Surface Science; 504:
429 144481.<https://doi.org/10.1016/j.apsusc.2019.144481>.
- 430 Ma D, et al., 2022.Enhanced Catalytic Ozonation for Eliminating CH_3SH via Stable and Circular
431 Electronic Metal-Support Interactions of Si-O-Mn Bonds with Low Mn Loading.Environ Sci
432 Technol; 56: 3678-3688.<https://doi.org/10.1021/acs.est.1c07065>.
- 433 Niu X, Lei Z, 2019.Copper doped manganese oxides to produce enhanced catalytic performance for CO
434 oxidation.Journal of Environmental Chemical Engineering; 7:
435 103055.<https://doi.org/10.1016/j.jece.2019.103055>.
- 436 Otto F, et al., 2013.Relative effects of enthalpy and entropy on the phase stability of equiatomic high-
437 entropy alloys.Acta Materialia; 61: 2628-2638.<https://doi.org/10.1016/j.actamat.2013.01.042>.
- 438 Polychronopoulou K, et al., 2021.Design Aspects of Doped CeO_2 for Low-Temperature Catalytic CO
439 Oxidation: Transient Kinetics and DFT Approach.ACS Appl Mater Interfaces; 13: 22391-

- 440 22415.<https://doi.org/10.1021/acsami.1c02934>.
- 441 Sacco NA, et al., 2022.One step citric acid-assisted synthesis of Mn-Ce mixed oxides and their
442 application to diesel soot combustion.Fuel; 322: 124201.<https://doi.org/10.1016/j.fuel.2022.124201>.
- 443 Schweke D, et al., 2018.The Interaction of CO₂ with CeO₂ Powder Explored by Correlating Adsorption
444 and Thermal Desorption Analyses.The Journal of Physical Chemistry C; 122: 9947-
445 9957.<https://doi.org/10.1021/acs.jpcc.8b01299>.
- 446 Tang XL, et al., 2020.Effect of hierarchical element doping on the low-temperature activity of
447 manganese-based catalysts for NH₃-SCR.Journal of Environmental Chemical Engineering; 8:
448 104399.<https://doi.org/10.1016/j.jece.2020.104399>.
- 449 Venkataswamy P, et al., 2015.Structural properties of alumina supported Ce–Mn solid solutions and their
450 markedly enhanced catalytic activity for CO oxidation.Applied Surface Science; 349: 299-
451 309.<https://doi.org/10.1016/j.apsusc.2015.04.220>.
- 452 Wan J, et al., 2022.Designed preparation of nano rod shaped CeO₂-MnO catalysts with different Ce/Mn
453 ratios and its highly efficient catalytic performance for chlorobenzene complete oxidation: New
454 insights into structure–activity correlations.Chemical Engineering Journal; 433:
455 133788.<https://doi.org/10.1016/j.cej.2021.133788>.
- 456 Wang B, et al., 2017.Plasma-catalytic removal of toluene over CeO₂ -MnO_x catalysts in an atmosphere
457 dielectric barrier discharge.Chemical Engineering Journal; 322: 679-
458 692.<https://doi.org/10.1016/j.cej.2017.03.153>.
- 459 Wang Y, et al., 2022.Mechanistic study of low-temperature CO oxidation over CuO/Cu₂O interfaces with
460 oxygen vacancy modification.Applied Surface Science; 603:
461 154469.<https://doi.org/10.1016/j.apsusc.2022.154469>.
- 462 Wei L, et al., 2021.Ce-promoted Mn/ZSM-5 catalysts for highly efficient decomposition of ozone.J
463 Environ Sci (China); 103: 219-228.<https://doi.org/10.1016/j.jes.2020.10.008>.
- 464 Yang J, et al., 2020.Iron doped effects on active sites formation over activated carbon supported Mn-Ce
465 oxide catalysts for low-temperature SCR of NO.Chemical Engineering Journal; 379:
466 122398.<https://doi.org/10.1016/j.cej.2019.122398>.
- 467 Yang ZY, et al., 2019.Study of reaction mechanism based on further promotion of low temperature
468 degradation of toluene using nano-CeO₂/Co₃O₄ under microwave radiation for cleaner production

- 469 in spraying processing. *Journal of Hazardous Materials*; 373: 321-
470 334. <https://doi.org/10.1016/j.jhazmat.2019.03.062>.
- 471 Yao XJ, et al., 2017. Influence of preparation methods on the physicochemical properties and catalytic
472 performance of MnO_x-CeO₂ catalysts for NH₃-SCR at low temperature. *Chinese Journal of Catalysis*;
473 38: 146-159. [https://doi.org/10.1016/s1872-2067\(16\)62572](https://doi.org/10.1016/s1872-2067(16)62572).
- 474 Ye Z, et al., 2022. Investigation of Cu-Mn catalytic ozonation of toluene: Crystal phase, intermediates
475 and mechanism. *J Hazard Mater*; 424: 127321. <https://doi.org/10.1016/j.jhazmat.2021.127321>.
- 476 Yu WT, et al., 2021. Facile treatment tuning the morphology of Pb with state-of-the-art selectivity in CO₂
477 electroreduction to formate. *Chemical Communications*; 57: 7418-
478 7421. <https://doi.org/10.1039/d1cc02113c>.
- 479 Zhang X-m, et al., 2016. Dynamic active sites over binary oxide catalysts: In situ/operando spectroscopic
480 study of low-temperature CO oxidation over MnO_x-CeO₂ catalysts. *Applied Catalysis B: Environmental*;
481 191: 179-191. <https://doi.org/10.1016/j.apcatb.2016.03.030>.
- 482 Zhang X, et al., 2021. The promoting effect of H₂O on rod-like MnCeO_x derived from MOF_s for toluene
483 oxidation: A combined experimental and theoretical investigation. *Applied Catalysis B: Environmental*;
484 297: 120393. <https://doi.org/10.1016/j.apcatb.2021.120393>.
- 485 Zhao L, et al., 2019. Synthesis of CeMnO_x hollow microsphere with hierarchical structure and its
486 excellent catalytic performance for toluene combustion. *Applied Catalysis B: Environmental*; 245:
487 502-512. <https://doi.org/10.1016/j.apcatb.2019.01.005>.
- 488 Zhao Y, et al., 2016. Inhibition of calcium sulfate scale by poly (citric acid). *Desalination*; 392: 1-
489 7. <https://doi.org/10.1016/j.desal.2016.04.010>.
- 490 Zhu L, et al., 2017. Cerium modified birnessite-type MnO₂ for gaseous formaldehyde oxidation at low
491 temperature. *Applied Catalysis B: Environmental*; 211: 212-
492 221. <https://doi.org/10.1016/j.apcatb.2017.04.025>.
- 493 Zhu T, et al., 2022. Multi-process and multi-pollutant control technology for ultra-low emissions in the
494 iron and steel industry. *Journal of Environmental Sciences*; 123: 83-
495 95. <https://doi.org/10.1016/j.jes.2022.01.044>.

496

Highlights

- The hydrothermal citrate complexation method enhanced the interaction between Ce-Mn and showed a superior performance for the oxidation of CO.

- The $\text{Mn}^{3+} + \text{Ce}^{4+} \leftrightarrow \text{Mn}^{4+} + \text{Ce}^{3+}$ redox cycle facilitates its synergistic effect in the CO oxidation process.

- The reaction of CO oxidation on Ce-Mn surface is proposed.

The authors declare that they have no known competing financial interests or personal relationships that could have appeared to influence the work reported in this paper.

Journal Pre-proof